

# Image Retrieval using Heat Diffusion for Deep Feature Aggregation

Shanmin Pang<sup>1</sup>, Jin Ma<sup>1</sup>, Jianru Xue<sup>1</sup>, Jihua Zhu<sup>1</sup>, Vicente Ordonez<sup>2</sup>

<sup>1</sup>Xi'an Jiaotong University, <sup>2</sup>University of Virginia

**Abstract.** Image-level feature descriptors obtained from convolutional neural networks have shown powerful representation capabilities for image retrieval. In this paper, we present an unsupervised method to aggregate deep convolutional features into compact yet discriminative image vectors by simulating the dynamics of heat diffusion. A distinctive problem in image retrieval is that repetitive or *bursty* features tend to dominate feature representations, leading to less than ideal matches. We show that by leveraging elegant properties of the heat equation, our method is able to select *informative* features while avoiding over-representation of *bursty* features. We additionally present a theoretical time complexity analysis showing the efficiency of our method, which is further demonstrated in our experimental evaluation. Finally, we extensively evaluate the proposed approach with pre-trained and fine-tuned deep networks on common public benchmarks, and show superior performance compared to previous work.

**Keywords:** Heat equation, Compact representations, Image retrieval

## 1 Introduction

Image retrieval has always been an attractive research topic in the field of computer vision. By allowing users to search similar images from a large database of digital images, it provides a natural and flexible interface for image archiving and browsing. Convolutional Neural Networks (CNNs) have shown remarkable accuracy in tasks such as image classification, and object detection. Recent research has also shown positive results of using CNNs on image retrieval [1,2,3]. However, unlike image classification approaches which often use global feature vectors produced by fully connected layers, these methods extract local features depicting image patches from the outputs of convolutional layers and aggregate these features into *compact* (a few hundred dimensions) image-level descriptors. Once meaningful and representative image-level descriptors are defined, visually similar images are retrieved by computing similarities between pre-computed database feature representations and query representations.

In this paper we devise a method to select *informative* features while avoiding over-representing *bursty* features. Inspired by an observation of similar phenomena in textual data, Jegou et al [4] identified *burstiness* as the phenomenon by which overly repetitive features within an instance tend to dominate the instance

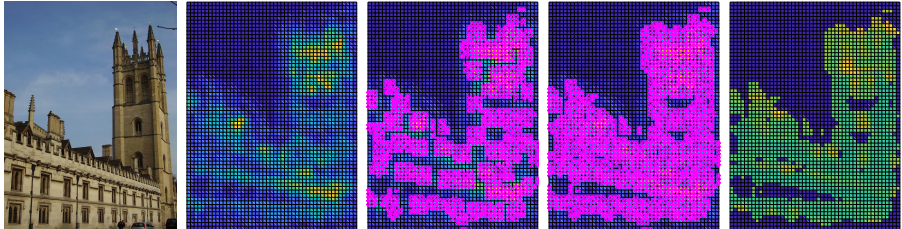


**Fig. 1.** An example visualization result of the proposed method with deep features extracted using the SiamMAC $\dagger$  [11] CNN model. From left to right: the original image; the corresponding map showing the matrix of summed responses from all feature maps (saliency scores); the detected ROIs (Section 3.1); locations for finally selected features (Section 3.2); and relative weights (warmer colors indicate larger weights) for selected features (Section 4). For instance, in this image, there seems to be distinctive areas at the top of the tower.

feature representation. In order to alleviate this issue, we propose a feature selection and aggregation approach that emulates the dynamics of heat diffusion. The idea is to model feature maps as a heat system where we weight highly the features leading to low system temperatures. This is because that these features are less connected to other features, and therefore they are more distinctive. The dynamics of the temperature in such system can be estimated using the partial differential equation induced by the heat equation. Fig. 1 shows a visualization of our feature selection, and feature weighting approach for an image.

Heat diffusion, and more specifically anisotropic diffusion, has been used successfully in various image processing and computer vision tasks. Ranging from the classical work of Perona and Malik [5] to further applications in image smoothing, image regularization, image co-segmentation, and optical flow estimation [6,7,8,9]. However, to our knowledge, it has not been applied to select and weight features from the outputs of a deep convolutional neural network. We show that by combining this classical image processing technique with a deep learning model, we are able to obtain significant gains against previous work. In contrast to some existing aggregation methods that either address informative feature selection [3] or bursty feature over-representation [2,10] individually, our method provides a unified solution.

Our contributions can be summarized as follows:

- Feature selection: Leveraging spatial information of local deep features, we develop a scheme to detect a subset of informative features corresponding to Region of Interests (ROIs), and then complete the whole feature selection process using the heat equation (Section 3).
- Feature weighting: By greedily considering each selected deep feature as a heat source and enforcing the temperature of the system be a constant within each heat source, we propose a novel efficient feature weighting approach to reduce the undesirable influence of *bursty* features (Section 4).
- By considering each query image as a heat source, we also produce an image re-ranking technique that leads to additional gains in performance. Finally,

we conduct extensive quantitative evaluations on commonly used image retrieval benchmarks, and demonstrate substantial performance improvement over existing unsupervised methods for feature aggregation (Section 5).

## 2 Related Work

Early attempts to use deep learning for image retrieval considered the use of the activations of fully connected layers as image-level descriptors [12,13,14]. In [12], a global representation was derived from the output of the penultimate layer. This work was among the first to show better performance than traditional methods based on SIFT-like features at the same dimensionality. Concurrently, Gong et al. [14] extracted multiple fully-connected activations by partitioning images into fragments, and then used VLAD-embeddings [15] to aggregate the activations into a single image vector. The work [13] reported promising results using sets of a few dozen features from the fully-connected layers of a CNN, without aggregating them into a global descriptor. However, observing that neural activations of the lower layers of a CNN capture more spatial details, later works advocated using the outputs of convolutional layers as features [1,2,3,16,17,18,19]. In our work, we follow this approach and use the outputs of the last convolutional layer of a pre-trained or fine-tuned convolutional neural network.

Considerable effort has been dedicated to aggregating the activations of convolutional layers into a distinctive global image vector. For instance, [17,18] evaluated image-level descriptors obtained using max-pooling over the last convolutional layer, while Babenko and Lempitsky [1] showed that sum-pooling leads to better performance. Kalantidis et al. [2] further proposed a non-parametric method to learn weights for both spatial locations and feature channels. Related to that, Hoang et al. [3] proposed several masking schemes to select a representative subset of local features before aggregation, and got satisfactory results by taking advantage of a triangulation embedding [20]. In another work, Tolias et al. [16] computed a collection of region vectors with max-pooling on the final convolutional layer, and then combined all region vectors into a final global representation. More recently, Xu et al. [19] independently employed selected part detectors to generate regional representations with weighted sum-pooling [2], and then concatenated regional vectors as the global descriptor. In our work, we instead propose heat diffusion to weight and then aggregate deep feature descriptors.

Fine-tuning an off-the-shell network is also popular for performance improvement. For instance, there are a number of approaches that learn features for the specific task of landmark retrieval [11,21,22,23]. While fine-tuning a pre-trained model is usually preceded by extensive manual annotation, Radenovic et al [11] introduced an unsupervised fine-tuning of CNN for image retrieval from a large collection of unordered images in a fully automated manner. Similar to [11], the works of [22,23] overcame laborious annotation, and collected training data in a weakly supervised manner. More specifically, Arandjelovic et al. [22] proposed a new network architecture, NetVLAD, that is trained for place recognition in an

end-to-end manner from weakly supervised Google Street View Time Machine images. Cao et al. [23] trained a special architecture Quartet-net by harvesting data automatically from GeoPair [24]. We show that our feature selection, weighting, and re-ranking approach, while not requiring extra supervision, performs favorably compared to these previous methods.

In a couple of very recent works [25,26], images were represented by multiple high-dimensional regional vectors. These two approaches achieve great performance on common benchmarks, they are however computationally demanding, both in terms of memory and computational usage. In contrast, our work uses a single vector representation while achieving similar performance.

### 3 Feature Selection using the Heat Equation

Given an input image  $I$  that is fed through a pre-trained or a fine-tuned CNN, the activations (responses) of a convolutional layer form a 3D tensor  $\mathbf{X} \in \mathbb{R}^{W \times H \times K}$ , where  $W \times H$  is the spatial resolution of the feature maps, and  $K$  is the number of feature maps (channels). We denote  $\Omega = \{\mathbf{f}_{ij}\}$  as a set of  $W \times H$  local features, where  $\mathbf{f}_{ij}$  is a  $K$ -dimensional vector at each position  $(i, j)$  in  $\mathbf{X}$ . We assume that Rectified Linear Units (ReLU) are applied as a last step, guaranteeing that all elements of  $\mathbf{f}_{ij}$  are non-negative.

#### 3.1 Selecting Regions of Interest (ROIs)

We first compute a *saliency map*  $\mathbf{S} \in \mathbb{R}^{W \times H}$  containing a sum of feature responses at each location such that:

$$S(i, j) = \sum_{k=1}^K f_{ij}(k), \quad 1 \leq i \leq W, \quad 1 \leq j \leq H, \quad (1)$$

where  $f_{ij}(k)$  is the  $k$ -th ( $1 \leq k \leq K$ ) element of  $\mathbf{f}_{ij}$ . Two recent papers [2,3] use this type of saliency map as a measure of feature *informativeness*. In [2], larger  $S(i, j)$  translates to a larger weighting coefficient for  $\mathbf{f}_{ij}$ ; while in [3],  $\mathbf{f}_{ij}$  is selected if  $S(i, j)$  is greater than a threshold. In other words, the weight for  $\mathbf{f}_{ij}$  is determined individually, and only based on the corresponding saliency value  $S(i, j)$ . Our method obtains further gains by leveraging spatial information.

We particularly observe that spatially consistent regions with large saliency values generally correspond to object instances. Thus, we select *non-overlapping* regions of interest  $\mathbf{R}_m$  such that the following conditions are met:

- Each region  $\mathbf{R}_m$  is generated around a central point along with its spatial neighbors within a distance  $\omega$  from the center.
- All saliency scores  $S(i, j)$  inside each region of interest, including the center, are above a threshold  $\tau$ .
- In our implementation we additionally allow ROIs not to be strictly rectangles by allowing the percentage of saliency scores in  $\mathbf{R}_m$  greater than a relaxation coefficient  $\eta \in (0, 1)$

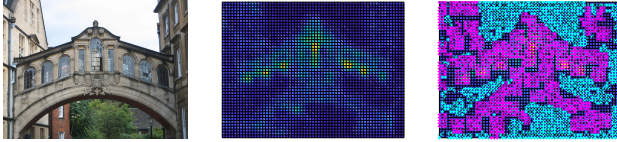


**Fig. 2.** On the left is the original image, on the center we show the saliency map as computed by Eq.(1), and on the right are ROIs and background points selected after our first pass as described in Section 3.1. Features in  $\mathbf{F}$  and  $\mathbf{B}$  are highlighted in magenta and cyan, respectively.

Obtaining these regions can be accomplished by a simple algorithm that uses a single pass over feature locations with the use of an additional indicator variable to mark visited locations. We begin with traversing the location that has the maximum saliency score, and locations with larger saliency scores are given priority to check. In each iteration the process keeps either getting a new ROI based on the constraints outlined above, or simply marking a point not to be a ROI center. From the previous ROI selection step we obtain a large portion of discriminative *foreground* features as follows:

$$\mathbf{F} = \{ \mathbf{f}_{ij} \mid (i, j) \in \mathbf{R}_F \}, \quad \mathbf{R}_F = \bigcup_{m=1}^M \mathbf{R}_m, \quad (2)$$

where  $M$  is the number of ROIs selected in the previous step. Compared to the ROI selection algorithm, the process of determining uninformative *background* features is rather simple. We consider features with saliency scores no greater than  $\tau$  as the current background features  $\mathbf{B}$ :

$$\mathbf{B} = \{ \mathbf{f}_{ij} \mid S(i, j) \leq \tau \}. \quad (3)$$

Fig. 2 shows the computed saliency map, and ROI as well as background outputs for a sample input image.

### 3.2 Re-assigning Undefined Features using the Heat Equation

So far we have assigned a subset of features in  $\Omega$  into either *foreground* features  $\mathbf{F}$ , or *background* features  $\mathbf{B}$ . However, there is a set of features  $\mathbf{U} = \Omega - \mathbf{F} - \mathbf{B}$  that have not been assigned to any of these two sets. In this section, we utilize the theory of anisotropic diffusion [27] to assign each deep feature in  $\mathbf{U}$  to either  $\mathbf{F}$  or  $\mathbf{B}$ .

We first transform each location  $(i, j)$  to one dimensional coordinate  $m = i + (j - 1) \times W$ . As a result, each  $\mathbf{f}_{ij} \in \Omega$  is rewritten as  $\mathbf{f}_m$ ,  $m = 1, 2, \dots, WH$ . Then let  $\mathcal{G} = (\mathcal{V}, \mathcal{E})$  denote an undirected graph, where  $\mathcal{V} = \{\mathbf{U}, \mathbf{f}_l\}$  is the set of nodes, and  $\mathbf{f}_l$  is a point in  $\mathbf{F}$ ; and  $\mathcal{E} = \{e(\mathbf{f}_m, \mathbf{f}_n), \forall (\mathbf{f}_m, \mathbf{f}_n) \in \mathcal{V}^2\}$  is the set of edges. Assume that the graph constitutes a heat transfer system where  $\mu_l(m, t)$  is the temperature at node  $\mathbf{f}_m$  at time  $t$ , and  $\mathbf{P}$  is a  $|\mathcal{V}| \times |\mathcal{V}|$  positive definite symmetric matrix called the *diffusion tensor*. Then the *heat equation* for this system is defined as follows:

$$\partial_t \boldsymbol{\mu} = \text{div}(\mathbf{P} \nabla \boldsymbol{\mu}) \quad (4)$$

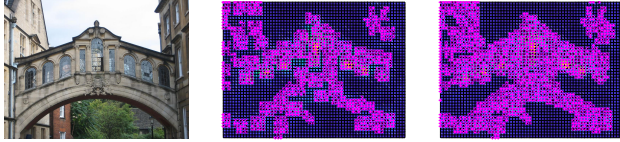


**Fig. 3.** On the left is the original image, on the center we show the selected ROIs after our first pass as described in Section 3.1, and on the right are the final features in  $\mathbf{F}$  after heat diffusion highlighted in magenta, Section 3.2.

Our problem is to compute the temperature at each node of  $\mathbf{U}$  that is under heat diffusion by assigning  $\mathbf{f}_l$  as the heat source. That is,

$$\begin{cases} \frac{\partial \mu_l(m,t)}{\partial t} = \text{div}(\mathbf{P} \nabla \mu_l(m,t)), \\ \text{s.t. } \mu_l(g) = 0, \mu_l(l) = 1, \end{cases} \quad (5)$$

where we use *Dirichlet* boundary conditions [27], and assume that the temperature of the environment node (outside of the system) and the source node is always zero (i.e.,  $\mu_l(g) = 0$ ) and one (i.e.,  $\mu_l(l) = 1$ ), respectively.

In practice, we compute the temperature at each node with the following simplified assumptions. Specifically, we let  $t \rightarrow +\infty$  and consequently drop  $t$  in our method as we are interested in the steady state, and define the diffusion tensor  $\mathbf{P}$  by *cosine* similarity between feature vectors:

$$P(m, n) = \begin{cases} 0, & m = n, \\ \frac{\mathbf{f}_m^T \mathbf{f}_n}{\|\mathbf{f}_m\| \|\mathbf{f}_n\|}, & m \neq n. \end{cases} \quad (6)$$

Furthermore, we assume that the dissipation heat loss at a node  $\mathbf{f}_m$  is  $\lambda_m$ , which is constant in time. In other words, each node  $\mathbf{f}_m \in \mathbf{U}$  is connected to an environment node  $g$  with diffusivity of  $\lambda_m$ . With these assumptions, the heat diffusion Eq.(5) reduces to the simplified version [27,28]:

$$\begin{cases} \mu_l(m) = \frac{1}{a_m} \sum P(m, n) \mu_l(n), \quad a_m = \sum P(m, n) + \lambda_m, \quad m \neq g, l, \\ \text{s.t. } \mu_l(g) = 0, \mu_l(l) = 1. \end{cases} \quad (7)$$

Without loss of generality, we assume  $\mathbf{P} = (\mathbf{P}_1, \mathbf{P}_2; \mathbf{P}_2^T, 0)$ , where  $\mathbf{P}_1 \in \mathbb{R}^{|\mathbf{U}| \times |\mathbf{U}|}$  stores the similarities between any two pair points in  $\mathbf{U}$ , and  $\mathbf{P}_2 \in \mathbb{R}^{|\mathbf{U}| \times 1}$  stores the similarities between points in  $\mathbf{U}$  and  $f_l$ . Thus, Eq.(7) can be rewritten as

$$\mu_l = (\mathbf{I} - \mathbf{A}^{-1} \mathbf{P}_1)^{-1} (\mathbf{A}^{-1} \mathbf{P}_2). \quad (8)$$

where  $\mathbf{I}$  is the identity matrix, and  $\mathbf{A} = \text{diag}(a_1, \dots, a_{|\mathbf{U}|})$  is the diagonal matrix.

We update  $\mathcal{V}$  by replacing  $\mathbf{f}_l \in \mathbf{F}$  one by one and repeat computing the temperature at each node  $\mathbf{f}_m \in \mathbf{U}$  with Eq.(8) until all points in  $\mathbf{F}$  are traversed. Then, we define the *temperature gain* of  $\mathbf{f}_m$  from the discriminative set  $\mathbf{F}$  as

$$\mu_F(m) = \max_{\mathbf{f}_l \in \mathbf{F}} \mu_l(m). \quad (9)$$

Similarly, we can also obtain the temperature gain of  $\mathbf{f}_m \in \mathbf{U}$  from the background set  $\mathbf{B}$  as  $\mu_B(m) = \max_{\mathbf{f}_l \in \mathbf{B}} \mu_l(m)$ .

Finally, we assign an unknown feature to foreground or background by comparing  $\mu_F(m)$  and  $\mu_B(m)$ . That is, for each point  $\mathbf{f}_m \in \mathbf{U}$ , we add it to  $\mathbf{F}$  if  $\mu_F(m) > \mu_B(m)$ ; otherwise, we add it to  $\mathbf{B}$ . Fig. 3 shows the final set of features in  $\mathbf{F}$  for a sample input image.

**Computing  $\mu_F(m)$  and  $\mu_B(m)$  in practice.** It is not necessary to repeat Eq.(8)  $|\mathbf{F}| + |\mathbf{B}|$  times to get the gains of  $\mathbf{f}_m$  from both  $\mathbf{F}$  and  $\mathbf{B}$ . Instead, we compute both  $\mu_F(m)$  and  $\mu_B(m)$  only one time. This is accomplished by extending  $\mathbf{P}_2$  to a  $|\mathbf{U}| \times (|\mathbf{F}| + |\mathbf{B}|)$  matrix, in which each entry denotes the cosine similarity between a pair points in  $\mathbf{U}$  and in  $\mathbf{F}$  or  $\mathbf{B}$ . The cost of computing the similarity matrix  $\mathbf{P}$  is in  $O(WHK|\mathbf{U}|)$ , and the cost of Eq.(8) is in  $O(|\mathbf{U}|^2WH)$ . Thus, the total complexity is in  $O(WH(K|\mathbf{U}| + |\mathbf{U}|^2))$ . Therefore the proposed feature selection process is efficient as all the values of  $W$ ,  $H$ ,  $K$  and  $|\mathbf{U}|$  are small in practice.

## 4 Feature Weighting using the Heat Equation

Once we have obtained the selected feature set  $\mathbf{F}$ , we utilize again the heat equation to compute a weighting for the features based on their distinctiveness, thus avoiding the *burstiness* issue. Without loss of generality, assume that  $\mathbf{F} = \{\mathbf{f}_1, \mathbf{f}_2, \dots, \mathbf{f}_{|\mathbf{F}|}\}$ . We greedily consider each point  $\mathbf{f}_l \in \mathbf{F}$  as a heat source, and compute the temperature of all the other points under the linear anisotropic diffusion equation Eq.(5). For simplicity, as performed in the previous section, we also use the following more specific equation:

$$\begin{cases} \mu_l(m) = \frac{1}{a_m} \sum P(m, n) \mu_l(n), \quad a_m = \sum P(m, n) + \lambda_m, \quad m \neq g, l, \\ s.t. \quad \mu_l(g) = 0, \quad \mu_l(l) = 1, \end{cases} \quad (10)$$

to compute temperature of each point, where with some confusion, we still denote the similarity matrix that contains similarities between points in  $\mathbf{F}$  as  $\mathbf{P}$ . Thus, the temperature of the system is

$$\psi_l = \sum_{m=1}^{|\mathbf{F}|} \mu_l(m). \quad (11)$$

The value of  $\psi_l$  can indicate whether  $\mathbf{f}_l$  is a frequent feature or a rare one. Intuitively, a *bursty* feature is densely connected to other features with high similarities, which consequently rises the temperature of the system. In contrast, a rare feature connects other features sparsely and therefore causes the system temperature to be low. Thus, in order to balance the influence between rare features and frequent ones, we enforce the temperature of the system be a constant by introducing a set of weighting coefficients  $w_l$ . That is,

$$w_l \times \psi_l = 1, \forall \mathbf{f}_l \in \mathbf{F}. \quad (12)$$

As a result,  $w_l$  is used to reduce the burstiness effects, and we accordingly compute the final image representation  $\mathbf{v}_I$  of each image  $I$  by

$$\mathbf{v}_I = \frac{\left( \sum_{l=1}^{|\mathbf{F}|} w_l \mathbf{f}_l \right)^\alpha}{\left\| \left( \sum_{l=1}^{|\mathbf{F}|} w_l \mathbf{f}_l \right)^\alpha \right\|}, \quad (13)$$

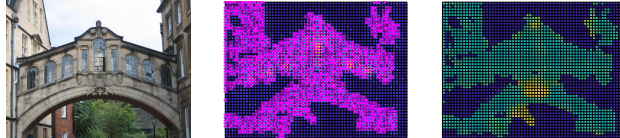


**Fig. 4.** On the left: original image, on the center: selected features in  $\mathbf{F}$  highlighted in magenta, Section 3, and on the right: weights computed using the heat equation, areas with low system temperature are weighted more (see Section 4). In the case of this image the base of the bridge seems to be the most distinctive area.

where  $0 < \alpha \leq 1$  is a constant, and we typically set  $\alpha = 0.5$ .  $\alpha$  plays the same role as the exponent parameter in the Power-law Normalization (PN) formula [29]. However, it is worth noting that, we apply  $\alpha$ -normalisation on the image vector *before* PCA whitening, while PN is integrated in the retrieval frameworks [10,30] *after* rotating the image representation with a PCA rotation matrix. Fig. 4 visualizes the weights computed for a sample input image, larger weights are shown in warmer colors.

#### 4.1 Computing Weights in Practice

We now turn to the problem of computing  $w_l$ . It seems that we have to solve Eq.(10)  $|\mathbf{F}|$  times to get the image representation of  $I$ , and each time we need to solve a linear equation of size  $(|\mathbf{F}| - 1) \times (|\mathbf{F}| - 1)$ . Thus, the total time cost is about in  $O(|\mathbf{F}|^4)$ . This might be computationally intensive if the selected feature set cardinality  $|\mathbf{F}|$  is large.

However, the actual time complexity can be reduced to  $O(|\mathbf{F}|^3)$ , and we can compute all  $\psi_l$  by inverting the matrix  $(\mathbf{I} - \mathbf{A}^{-1}\mathbf{P})$  only once. Specifically, we take computing  $\psi_1$  as an example to illustrate the practical computational process. We leverage the block structure of  $(\mathbf{I} - \mathbf{A}^{-1}\mathbf{P})$ , i.e.,

$$\mathbf{I} - \mathbf{A}^{-1}\mathbf{P} = \begin{bmatrix} 1 & -\mathbf{x}^T \\ -\mathbf{y} & \mathbf{Q} \end{bmatrix}, \quad (14)$$

where  $\mathbf{x}$  and  $\mathbf{y}$  are vectors of size  $|\mathbf{F}| - 1$ , and  $\mathbf{Q}$  is the matrix of size  $(|\mathbf{F}| - 1) \times (|\mathbf{F}| - 1)$ . According to Eqs. (8) and (11), it is easy to know that

$$\psi_1 = \sum \mathbf{Q}^{-1}\mathbf{y} + 1. \quad (15)$$

With the property of the block matrix, we have

$$(\mathbf{I} - \mathbf{A}^{-1}\mathbf{P})^{-1} = \begin{bmatrix} 1 + \mathbf{x}^T(\mathbf{Q} - \mathbf{y}\mathbf{x}^T)^{-1}\mathbf{y} & \mathbf{x}^T(\mathbf{Q} - \mathbf{y}\mathbf{x}^T)^{-1} \\ (\mathbf{Q} - \mathbf{y}\mathbf{x}^T)^{-1}\mathbf{y} & (\mathbf{Q} - \mathbf{y}\mathbf{x}^T)^{-1} \end{bmatrix}. \quad (16)$$

Furthermore, one can prove that

$$\mathbf{Q}^{-1}\mathbf{y} = \frac{(\mathbf{Q} - \mathbf{y}\mathbf{x}^T)^{-1}\mathbf{y}}{1 + \mathbf{x}^T(\mathbf{Q} - \mathbf{y}\mathbf{x}^T)^{-1}\mathbf{y}}. \quad (17)$$

The above three equations demonstrate that we can derive  $\psi_1$  by using the first column of  $(\mathbf{I} - \mathbf{\Lambda}^{-1}\mathbf{P})^{-1}$ . Similarly, we can get  $\psi_l$  using the  $l$ -th column of  $(\mathbf{I} - \mathbf{\Lambda}^{-1}\mathbf{P})^{-1}$ :  $\psi_l = \frac{\sum_{m=1, m \neq l}^{|F|} (\mathbf{I} - \mathbf{\Lambda}^{-1}\mathbf{P})^{-1}(m, l)}{(\mathbf{I} - \mathbf{\Lambda}^{-1}\mathbf{P})^{-1}(l, l)} + 1$ . Thus, the conclusion that the computational cost is in  $O(|F|^3)$  holds.

## 5 Experiments and Results

### 5.1 Datasets and Evaluation Protocol

We evaluate our method on three public datasets: **Oxford Buildings** (Oxford5k) [31], **Paris** (Paris6k) [32], and **INRIA Holidays** (Holidays) [33].

**Oxford5k** contains a set of 5,062 photographs comprising 11 different Oxford landmarks. There are 55 query images with each 5 queries corresponding to a landmark. Following the standard protocol, we crop the query images based on the provided bounding boxes before retrieval. The performance is measured using mean average precision (mAP) over the 55 queries, where *junk* images are removed from the ranking.

**Paris6k** consists of 6,392 high resolution images of the city Paris. This dataset also provides 55 query images and their corresponding ground truth relevant images. We also use cropped query images to perform retrieval, and measure the overall retrieval performance using mAP.

**Holidays** includes 1,491 images in total, and selects 500 images as queries associated with the 500 partitioning groups of the image set. To be directly comparable with recent works [1,2,3], we manually fix images in the wrong orientation by rotating them by  $\pm 90$  degrees. The retrieval quality is also measured using mAP over 500 queries, with the query removed from the ranked list.

**Flickr100k** [31] was crawled from Flickr’s 145 most popular tags and consists of 11,071 images. We combine these 100k distractor images with Oxford5k and Paris6k, and produce a Oxford105k and Paris106k datasets respectively. In this way, we evaluate the behavior of our method at a larger scale.

### 5.2 Implementation Notes

**Deep convolutional features.** In order to extensively evaluate our method, we use a pre-trained and two fine-tuned deep neural networks to extract multiple convolutional features for each image. The adopted pre-trained network is VGG16 [34], which is widely used in the literature. We use two fine-tuned versions of VGG16: NetVLAD $\star$  [22], and siaMAC $\dagger$  [11].

Following the practice of previous works [2,11], we choose the last convolutional layer of each network to separately extract patch-level image features. We use public available trained models. Specifically, we use the Matconvnet toolbox [35] for VGG16, and use models provided in [22] and [11] for NetVLAD $\star$  and siaMAC $\dagger$ , respectively. In addition, in order to accelerate feature extraction, we resize the longest side of all images to 1,024 pixels while preserving aspect ratios before using them as input to each deep network.

**Table 1.** mAP performance (in %) on Oxford5k with different  $\omega$  values. Note  $\eta = 0.5$  in this table.

$\omega$	3	5	7	9	11
mAP	82.7	83.0	82.6	82.4	82.2

**Table 2.** The mAP performance (in %) on Oxford5k with different  $\eta$  values which controls the shape of the ROI selection areas. Note:  $\omega = 5$  in this table.

$\eta$	0.3	0.5	0.7	0.9	1.0
mAP	82.2	83.0	82.8	82.4	82.4

**PCA whitening** is widely used in many image retrieval systems [36,2,3,1] as it can effectively improve the discriminative ability of image vectors. In order to avoid over-fitting, the PCA matrix is usually learned with the set of aggregated image vectors produced from a held-out dataset. To be directly comparable with related works, we learn PCA parameters on Paris6k for Oxford5k and Oxford105k, and on Oxford5k for Paris6k and Paris106k. As for Holidays, we randomly select a subset of 5000 images from Flickr100k to learn parameters.

**Post-processing.** It is well-known that Query Expansion (QE) [37] is an effective post-processing technique to increase retrieval performance. Given the ranked list of database images over a query image, we simply calculate the average vector of the 10 top-ranked image vectors and the query vector, and we then use the  $L_2$  normalized average vector to re-query again.

Additionally we propose a heat re-ranking approach where we consider the query as the heat source, and re-rank 500 top-ranked images by computing their temperatures with Eq.(10). We refer to this re-ranking as HeR, and apply it on our retrieval system with and without QE. In our setup, both QE and HeR are efficient in practice.

### 5.3 Analysis of Parameter Impact

The ROI detection step introduces three parameters: threshold  $\tau$ , window size  $\omega$ , and a relaxation coefficient  $\eta$  which controls how rectangular are the ROI areas. We evaluate the retrieval performance of our method for different settings of parameters with deep convolutional features extracted using siaMAC†.

**Parameter  $\tau$**  is a threshold to determine whether a feature is *informative* or not. To generalize and avoid over-fitting, we learn  $\tau$  with held-out datasets. We use the same held-out sets that we used for estimating the PCA matrix. Specifically, for Oxford5k and Oxford105k (Paris6k and Paris106k), we set  $\tau$  to the median value of saliency scores from Paris6k (Oxford5k). Similarly, we choose  $\tau$  for Holidays using the selected subset from Flickr100k.

**Impact of  $\omega$ .** The mAP performance on Oxford5k under different  $\omega$  values with  $\eta = 0.5$  is shown in Table 1. As shown, our method is insensitive to  $\omega$ , and the performance gap between the maximum and minimum mAP values is less than 1%. We select  $\omega = 5$  in the following experiments as it gives the best result.

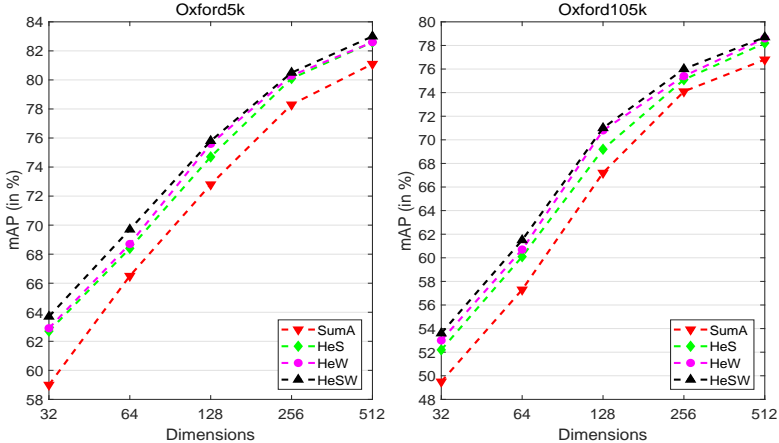


**Fig. 5.** Justifying the effect of each step that is contained in our method under different dimensions of image vectors. Short representations are achieved by keeping only the first components of 512 dimensional image vectors after PCA whitening.

**Table 3.** CPU timings (in seconds) for generating image representations. We do not include the cost of deep feature extraction.

Method	SumA	HeS	HeW	HeSW
CPU timings	0.013	0.104	0.193	0.171

**Impact of  $\eta$ .** Table 2 shows the retrieval performance by varying the relaxation coefficient  $\eta$ . As illustrated, when the value of  $\eta$  increases, the performance first slightly increases and then keeps stable with a little drop. The maximal mAP value is obtained with  $\eta = 0.5$ . Hence, we set  $\eta = 0.5$  in the rest of experiments.

**Impact of each step.** We illustrate mAP curves on Oxford5k and Oxford105k when varying the dimensionality of the final image vectors from 32 to 512 in Fig.5. Dimensionality reduction is achieved by keeping only the first  $D$  components of 512 dimensional image vectors after PCA whitening. In order to justify the contribution of each step that is contained in our method, we evaluate the performance of our method by taking them out of the pipeline. HeSW refers to our complete approach with both feature selection and feature weighting, while HeW and HeS mean we only perform feature weighting and feature selection, respectively. SumA means we obtain representations by simply summing all the features of each image, thus not performing neither feature selection nor feature weighting.

As we see, the gain of HeSW over SumA is about 2% in mAP on both Oxford5k and Oxford105k at  $D = 512$ . Furthermore, the performance gain is increasing with the reduction of the number of dimensions, and the gain is more than 4% at  $D = 32$ . Although HeW has nearly the same performance as HeSW at  $D \geq 128$ , it falls behind the latter with extremely short dimensions ( $D = 32, 64$ ). Moreover, it should be noted that HeW consistently outperforms HeS, although the margin is negligible in most cases.

**Table 4.** Performance (in mAP) comparison with methods using SIFT and off-the-shell available networks. We do not perform query expansion nor feature selection on Holidays as each query only has a few ground truth similar images, and many images from this dataset have no clear objects.

Feature	Method	Dim.	Ox5k	Ox105k	Pa6k	Pa106k	Holidays
SIFT	F-FAemb [30]	7,245	66.1	64.3	—	—	75.5
	Temb [10]	8,064	70.0	64.4	—	—	71.6
Fully connected layer	MOP-CNN [14]	2,048	—	—	—	—	80.8
	Neural codes [12]	4,096	54.5	51.2	—	—	79.3
	CNNaug-ss [13]	4,096	68.0	—	79.5	—	84.3
Deep Conv. layer of VGG16	R-MAC [16]	512	66.9	61.6	<b>83.0</b>	75.7	—
	CroW [2]	512	70.8	65.3	79.7	72.2	85.1
	MAX-mask [3]	512	65.7	60.5	81.6	72.4	85.0
	PWA [19]	512	72.0	66.2	82.3	<b>75.8</b>	—
	HeSW	512	<b>73.2</b>	<b>68.3</b>	82.0	74.0	<b>88.4</b>
	R-MAC+AML+QE [16]	512	<b>77.3</b>	73.2	86.5	79.8	—
	CroW+QE [2]	512	74.9	70.6	84.8	79.4	—
	PWA+QE [19]	512	74.8	72.5	86.0	80.7	—
	HeSW+QE	512	77.1	<b>75.4</b>	<b>86.6</b>	<b>82.4</b>	—
	HeSW+HeR	512	75.9	70.6	84.7	76.7	—
	HeSW+QE+HeR	512	78.2	77.3	87.9	83.6	—

Table 3 reports timings (excluding time for feature extraction) measured to compute image representations for different combinations of the proposed approach. We implement our method in Matlab, and plan to release our code for future comparisons. Benchmarks are obtained on an Intel Xeon E5-2630/2.20GHz with 20 cores. We report CPU timings which are larger than elapsed ones because CPU time takes into account all active threads. As Table 3 shows, the baseline method SumA is the most efficient one, and it is faster than the other three combinations by about an order of magnitude. HeS is more efficient than HeSW, which is more efficient than HeW, but the efficiency gap is small. The number of features for an image of size  $1,024 \times 768$  is 3,072, and the timing is typically 0.17s per image for HeSW. This indicates our method is fast in practice.

## 5.4 Comparison with the State-of-the-art

**Comparison with methods using SIFT and pre-trained networks.** In Table 4, we present comparisons of our approach using VGG16 with methods using SIFT and off-the-shell available networks, which utilize global representations of images. The comparison results are summarized as follows:

- Our approach significantly outperforms two state-of-the-art methods [30,10] using weaker SIFT features, although their dimensions are more than 10 times higher than ours. Furthermore, it also shows clear advantages over [14,12,13] that utilize fully connected layers to derive image representations.
- Compared with [16,2,3,19] which are also using the VGG16 model, our method achieves the best results on Oxford5k, Oxford105k and Holidays.

**Table 5.** Performance (in mAP) comparison with the state-of-the-art methods using unsupervised fine-tuned networks.

Method	Dim.	Ox5k	Ox105k	Pa6k	Pa106k	Holidays
NetVLAD [22]	512	67.6	–	74.9	–	86.1
siaMAC†+MAC [11]	512	79.0	73.9	82.4	74.6	79.5
siaMAC†+R-MAC [11]	512	77.0	69.2	83.8	76.4	82.5
siaMAC†+MAX-mask [3]	512	77.7	72.7	83.2	76.5	86.3
Fisher Vector [38]	512	81.5	76.6	82.4	–	–
NetVLAD★+HeSW	512	71.3	66.8	81.6	74.6	<b>87.4</b>
siaMAC†+HeSW	512	<b>83.0</b>	<b>78.7</b>	<b>86.8</b>	<b>80.9</b>	87.1
siaMAC†+MAC [11]	256	77.4	70.7	80.8	72.2	77.3
siaMAC†+R-MAC [11]	256	74.9	67.5	82.3	74.1	81.4
siaMAC†+HeSW	256	<b>80.3</b>	<b>75.6</b>	<b>85.2</b>	<b>79.2</b>	<b>85.9</b>
siaMAC†+MAC [11]	128	75.8	68.6	77.6	68.0	73.2
siaMAC†+R-MAC [11]	128	72.5	64.3	78.5	69.3	79.3
siaMAC†+HeSW	128	<b>75.8</b>	<b>70.8</b>	<b>81.3</b>	<b>74.6</b>	<b>85.0</b>
siaMAC†+MAC+R+QE [11]	512	85.0	81.8	86.5	78.8	–
siaMAC†+R-MAC+R+QE [11]	512	82.9	77.9	85.6	78.3	–
NetVLAD★+HeSW+QE	512	75.7	73.1	86.0	81.7	–
siaMAC†+HeSW+QE	512	<b>88.6</b>	<b>86.5</b>	<b>90.6</b>	<b>86.4</b>	–
siaMAC†+HeSW+QE	256	86.6	84.0	89.3	84.9	–
siaMAC†+HeSW+QE	128	80.7	77.3	86.0	80.7	–
NetVLAD★+HeSW+HeR	512	73.6	68.5	83.9	76.9	–
NetVLAD★+HeSW+QE+HeR	512	77.5	75.2	87.2	82.7	–
siaMAC†+HeSW+HeR	512	84.6	81.3	89.3	83.2	–
siaMAC†+HeSW+QE+HeR	512	89.8	88.2	92.0	87.7	–

Additionally, it is worth noting that, the gain on Holidays is over 3% at the same dimensionality.

- When combined with query expansion, our approach outperforms others on Oxford105k, Paris6k and Paris106k, and slightly falls behind [16] on Oxford5k. It should be noted that [16] includes a nontrivial and computationally intensive spatial verification process.
- The byproduct re-ranking strategy HeR gives a boost of nearly 3% in mAP on all evaluated datasets. Furthermore, it is complementary to QE, as applying it after QE produces the best results.

**Comparison with methods using fine-tuned networks.** We perform comparisons with recent unsupervised fine-tuned methods [22,11,3,38] in Table 5. The table again demonstrates the superior performance of our approach over related baselines at the same dimensionality:

- We establish new state-of-the-art results on all evaluated datasets at dimensionality of 512, and the improved mAP values are not negligible. For example, the gain on Paris106k is at least 4.4%.
- On the whole, the features extracted by siaMAC† are much stronger than those extracted by NetVLAD★. As shown, siaMAC†+HeSW is only slightly

**Table 6.** Comparison with the best results reported in the literature.

Method	Dim.	Ox5k	Ox105k	Pa6k	Pa106k	Holidays
Tolias et al. [39]		87.9	—	85.4	—	85.0
Mikulik et al. [40]		84.9	82.4	79.5	77.3	75.8
Tolias and Jégou [41]		89.4	84.0	82.8	—	—
Arandjelovic et al. [22]	4,096	71.6	—	79.7	—	87.5
Hoang et al. [3]	4,096	83.8	80.6	88.3	83.1	<b>92.2</b>
Iscen et al. [25]	5×512	91.5	84.7	<b>95.6</b>	<b>93.0</b>	—
Iscen et al. [26]	5×512	<b>91.6</b>	86.5	95.6	92.4	—
Gordo et al [21]	512	89.1	87.3	91.2	86.8	89.1
This paper	512	89.8	<b>88.2</b>	92.0	87.7	88.4

inferior to NetVLAD\*+HeSW on Holidays, and is obviously superior to the latter on the other datasets.

- With the same siameseMAC† features, our approach improves two related baselines R-MAC and MAC presented in [11] without and with dimensionality reduction, and the improvement is more significant on two large datasets: Oxford105k and Paris106k.
- Our method, HeSW, also produces much better results than [11] after query expansion, although [11] uses more sophisticated post-processing than us. Additionally, HeSW outperforms the best competing method at  $D = 256$ , and keeps competitive even at  $D = 128$ . Finally, we further enlarge the mAP gains over the compared methods by applying HeR after QE.

**Comparison with the best reported results.** Table 6 compares our best results with the very best results obtained with other methods that focus on spatial verification or use other VGG16-based learning models. Some of them [39,40,41,25,26] do not necessarily rely on a global representation, and some others [22,3] represent images with much higher dimensional vectors, and are thus not directly comparable. There is no doubt that these methods use a larger memory footprint than our approach. Compared with these methods, we still produce the best result on Oxford105k. Similar to our approach, the supervised fine-tuned method [21] also represents images with 512-D vectors. Compared with this method, we produce slightly inferior result on Holidays, and achieve better performance on the other datasets.

## 6 Conclusions

We proposed an approach for building compact but powerful image representations, and demonstrated its effectiveness on the task of instance-level retrieval. The approach integrates feature selection, feature weighting and re-ranking into a unified framework by utilizing the heat equation. Our method is unsupervised, and can be compatible with different CNNs, including pre-trained and fine-tuned networks. With the generated image representations, we establish new state-of-the-art results on public image retrieval benchmarks using 512-dimensional vector representations.

## References

1. Babenko, A., Lempitsky, V.: Aggregating local deep features for image retrieval. In: ICCV. (2015) 1269–1277
2. Kalantidis, Y., Mellina, C., Osindero, S.: Cross-dimensional weighting for aggregated deep convolutional features. In: ECCV Workshops. (2016) 685–701
3. Hoang, T., Do, T.T., Tan, D.K.L., Cheung, N.M.: Selective deep convolutional features for image retrieval. In: ACM MM. (2017) 1600–1608
4. Jégou, H., Douze, M., Schmid, C.: On the burstiness of visual elements. In: CVPR. (2009) 1169–1176
5. Perona, P., Malik, J.: Scale-space and edge detection using anisotropic diffusion. IEEE TPAMI **12**(7) (1990) 629–639
6. Zhang, J., Zheng, J., Cai, J.: A diffusion approach to seeded image segmentation. In: CVPR. (2010) 2125–2132
7. Tschumperle, D., Deriche, R.: Vector-valued image regularization with PDEs: A common framework for different applications. IEEE TPAMI **27**(4) (2005) 506–517
8. Kim, G., Xing, E.P., Fei-Fei, L., Kanade, T.: Distributed cosegmentation via submodular optimization on anisotropic diffusion. In: ICCV. (2011) 169–176
9. Bruhn, A., Weickert, J., Schnörr, C.: Lucas/kanade meets horn/schunck: Combining local and global optic flow methods. IJCV **61**(3) (2005) 211–231
10. Murray, N., Jégou, H., Perronnin, F., Zisserman, A.: Interferences in match kernels. IEEE TPAMI **39**(9) (2017) 1797–1810
11. Radenović, F., Tolias, G., Chum, O.: CNN image retrieval learns from BoW: Unsupervised fine-tuning with hard examples. In: ECCV. (2016) 3–20
12. Babenko, A., Slesarev, A., Chigorin, A., Lempitsky, V.: Neural codes for image retrieval. In: ECCV. (2014) 584–599
13. Razavian, A.S., Azizpour, H., Sullivan, J., Carlsson, S.: CNN features off-the-shelf: an astounding baseline for recognition. In: CVPR Workshops. (2014) 512–519
14. Gong, Y., Wang, L., Guo, R., Lazebnik, S.: Multi-scale orderless pooling of deep convolutional activation features. In: ECCV. (2014) 392–407
15. Jégou, H., Douze, M., Schmid, C., Pérez, P.: Aggregating local descriptors into a compact image representation. In: CVPR. (2010) 3304–3311
16. Tolias, G., Sicre, R., Jégou, H.: Particular object retrieval with integral max-pooling of CNN activations. In: ICLR. (2016) 1–12
17. Azizpour, H., Razavian, A.S., Sullivan, J., Maki, A., Carlsson, S.: From generic to specific deep representations for visual recognition. In: CVPR DeepVision Workshop. (2015) 36–45
18. Razavian, A.S., Sullivan, J., Carlsson, S., Maki, A.: Visual instance retrieval with deep convolutional networks. ITE Transactions on Media Technology and Applications **4**(3) (2016) 251–258
19. Xu, J., Shi, C., Qi, C., Wang, C., Xiao, B.: Unsupervised partbased weighting aggregation of deep convolutional features for image retrieval. In: AAAI. (2018) 1–8
20. Jégou, H., Zisserman, A.: Triangulation embedding and democratic aggregation for image search. In: CVPR. (2014) 3310–3317
21. Gordo, A., Almazán, J., Revaud, J., Larlus, D.: Deep image retrieval: Learning global representations for image search. In: ECCV. (2016) 241–257
22. Arandjelovic, R., Gronat, P., Torii, A., Pajdla, T., Sivic, J.: NetVLAD: CNN architecture for weakly supervised place recognition. In: CVPR. (2016) 5297–5307

23. Cao, J., Huang, Z., Wang, P., Li, C., Sun, X., Shen, H.T.: Quartet-net learning for visual instance retrieval. In: ACM MM. (2016) 456–460

24. Thomee, B., Shamma, D.A., Friedland, G., Elizalde, B., Ni, K., Poland, D., Borth, D., Li, L.J.: YFCC100M: the new data in multimedia research. *Communications of the ACM* **59**(2) (2016) 64–73

25. Iscen, A., Tolias, G., Avrithis, Y., Furion, T., Chum, O.: Efficient diffusion on region manifolds: Recovering small objects with compact CNN representations. In: CVPR. (2017) 926–935

26. Iscen, A., Tolias, G., Avrithis, Y., Furion, T., Chum, O.: Fast spectral ranking for similarity search. arXiv preprint arXiv:1703.06935 (2017)

27. Weickert, J.: Anisotropic diffusion in image processing. Teubner Stuttgart (1998)

28. Grady, L.: Random walks for image segmentation. *IEEE TPAMI* **28**(11) (2006) 1768–1783

29. Perronnin, F., Sánchez, J., Mensink, T.: Improving the fisher kernel for large-scale image classification. In: ECCV. (2010) 143–156

30. Do, T.T., Cheung, N.M.: Embedding based on function approximation for large scale image search. *IEEE TPAMI* **99** (2017) 1–12

31. Philbin, J., Chum, O., Isard, M., Sivic, J., Zisserman, A.: Object retrieval with large vocabularies and fast spatial matching. In: CVPR. (2007) 1–8

32. Philbin, J., Chum, O., Isard, M., Sivic, J., Zisserman, A.: Lost in quantization: Improving particular object retrieval in large scale image databases. In: CVPR. (2008) 1–8

33. Jégou, H., Douze, M., Schmid, C.: Improving bag-of-features for large scale image search. *IJCV* **87**(3) (2010) 316–336

34. Simonyan, K., Zisserman, A.: Very deep convolutional networks for large-scale image recognition. arXiv preprint arXiv:1409.1556 (2014)

35. Vedaldi, A., Lenc, K.: Matconvnet: Convolutional neural networks for MATLAB. In: ACM MM. (2015) 689–692

36. Jégou, H., Chum, O.: Negative evidences and co-occurrences in image retrieval: The benefit of PCA and whitening. In: ECCV. (2012) 774–787

37. Chum, O., Philbin, J., Sivic, J., Isard, M., Zisserman, A.: Total recall: Automatic query expansion with a generative feature model for object retrieval. In: ICCV. (2007) 1–8

38. Ong, E.J., Husain, S., Bober, M.: Siamese network of deep fisher-vector descriptors for image retrieval. arXiv preprint arXiv:1702.00338 (2017)

39. Tolias, G., Avrithis, Y., Jégou, H.: To aggregate or not to aggregate: Selective match kernels for image search. In: ICCV. (2013) 1401–1408

40. Mikulik, A., Perdoch, M., Chum, O., Matas, J.: Learning vocabularies over a fine quantization. *IJCV* **103**(1) (2013) 163–175

41. Tolias, G., Jégou, H.: Visual query expansion with or without geometry: Refining local descriptors by feature aggregation. *Pattern Recognition* **47**(10) (2015) 3466–3476